remote sensing

MDPI

Review

Remote Sensing Applications for Landslide Monitoring and Investigation in Western Canada

Renato Macciotta * and Michael T. Hendry

Department of Civil and Environmental Engineering, University of Alberta, Edmonton, AB T6G 2R3, Canada; hendry@ualberta.ca

* Correspondence: macciott@ualberta.ca

Abstract: Transportation infrastructure in mountainous terrain and through river valleys is exposed to a variety of landslide phenomena. This is particularly the case for highway and railway corridors in Western Canada that connect towns and industries through prairie valleys and the Canadian cordillera. The fluidity of these corridors is important for the economy of the country and the safety of workers, and users of this infrastructure is paramount. Stabilization of all active slopes is financially challenging given the extensive area where landslides are a possibility, and monitoring and minimization of slope failure consequences becomes an attractive risk management strategy. In this regard, remote sensing techniques provide a means for enhancing the monitoring toolbox of the geotechnical engineer. This includes an improved identification of active landslides in large areas, robust complement to in-place instrumentation for enhanced landslide investigation, and an improved definition of landslide extents and deformation mechanisms. This paper builds upon the extensive literature on the application of remote sensing techniques and discusses practical insights gained from a suite of case studies from the authors' experience in Western Canada. The review of the case studies presents a variety of landslide mechanisms and remote sensing technologies. The aim of the paper is to transfer some of the insights gained through these case studies to the reader.

Keywords: remote sensing; landslide monitoring; geotechnical investigation; risk management

Citation: Macciotta, R.; Hendry, M.T. Remote Sensing Applications for Landslide Monitoring and Investigation in Western Canada. *Remote Sens.* **2021**, *13*, 366. https://doi.org/10.3390/rs13030366

Received: 16 December 2020
Accepted: 19 January 2021
Published: 21 January 2021

1. Introduction

The integrity of the transportation network in Western Canada for securing uninterrupted fluidity of goods and people through the network are essential for the economy of the region. Transportation corridors through the Canadian Cordillera and through river valleys in the prairies are exposed to natural slope instabilities and steep cuts required to accommodate railroads and highways, where slope-related hazards are common. Landslide types in these regions include rock falls, rock slides and topples, earth flows, deep seated rotational and translational soil landslides, and compound landslides [1–6]. In this regard, a robust approach to manage the risks associated with landslides in natural and cut slopes becomes essential.

The risk management framework for landslides in natural and cut slopes has been previously discussed elsewhere [7–11]. After defining the scope of analysis, the framework requires characterizing the magnitude and likelihood of the slope failure, as well as the magnitude and likelihood of the potential consequences, which become the basis for estimating risk (combination of likelihood and consequence for each failure scenario analyzed). The level of risk calculated in this risk analysis (qualitative or quantitative) is evaluated against some adopted criteria to define its tolerability (risk assessment). The outcome of the risk assessment informs decision-making regarding the requirement for risk mitigation and control strategies (e.g., protection, stabilization, early warning), as well as the need for increased knowledge of the slope physical characteristics (e.g., geology, groundwater), failure mechanisms and potential triggers; and monitoring requirements for managing

residual risks. This is where remote sensing techniques become provide increased benefit to in-place instrumentation, particularly given the more frequent adoption of quantitative risk analyses since the late 1990s and early 2000's [12–15]. This risk management framework is illustrated in Figure 1 [11].

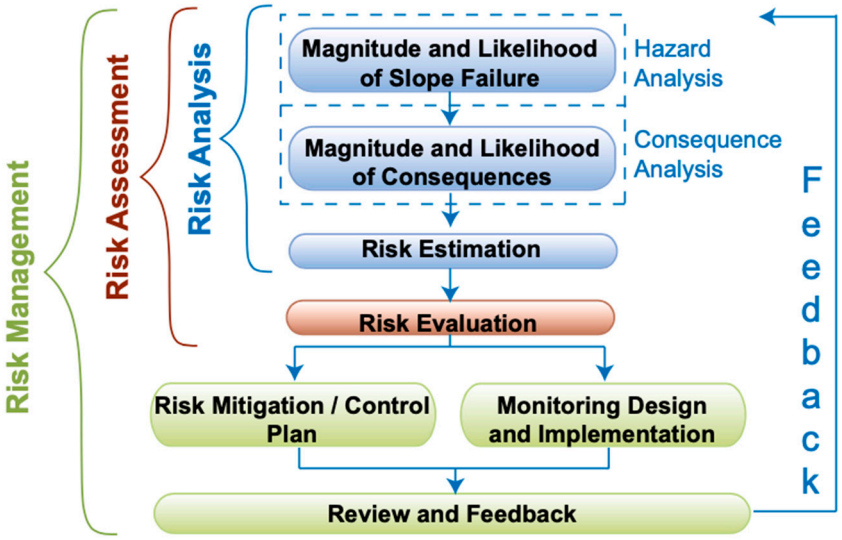

Figure 1. General risk management framework for landslides in natural and cut slopes. After [11].

Within the risk management framework in Figure 1, monitoring plays a fundamental role. Not only is robust monitoring the cornerstone of effective early warning, but also fundamental for increased understanding of the landslide mechanisms, kinematics and triggers. In this regard, remote sensing technologies have continued to develop to the point where they are becoming routine practice for landslide monitoring and for landslide investigation as part of the hazard analysis in Figure 1 [16]. These include ground-based and airborne (from manned and unmanned aircrafts) photogrammetry, laser scanning, and satellite and ground-based radar interferometry [17–28].

This paper presents a review of six case studies in Western Canada from the authors' experience; where remote sensing was used in combination with other site investigation and monitoring technologies to gain understanding of the slope deformation mechanisms and develop early warning systems. A brief description of the geologic context, landslide extents and deformation patterns are followed by a description of the instrumentation and remote sensing techniques deployed and the insights gained. It is noted that the work presented here reflects the methods that were considered most suited for the case studies discussed, which may vary in other contexts and for other jurisdictions. This work is not an exhaustive literature review of remote sensing techniques for landslide investigation; however, it presents valuable examples for how the information captured from remote sensing techniques enhance the implementation of the landslide risk management framework.

2. Chin Coulee Landslide

2.1. Location and Geology

The Chin Coulee landslide is located near the town of Taber in southern Alberta, Canada. The landslide is within a broad valley that was dammed to develop the Chin Coulee water reservoir. The landslide was likely triggered by a combination of the works required to relocate Highway 36 from near the toe of the slope to the crest of the slope (which required fill placement in the upper part of the slope) and filling of the reservoir [29–31]. The location of the Chin Coulee landside and an aerial view are shown in Figure 2 (modified from [30]).

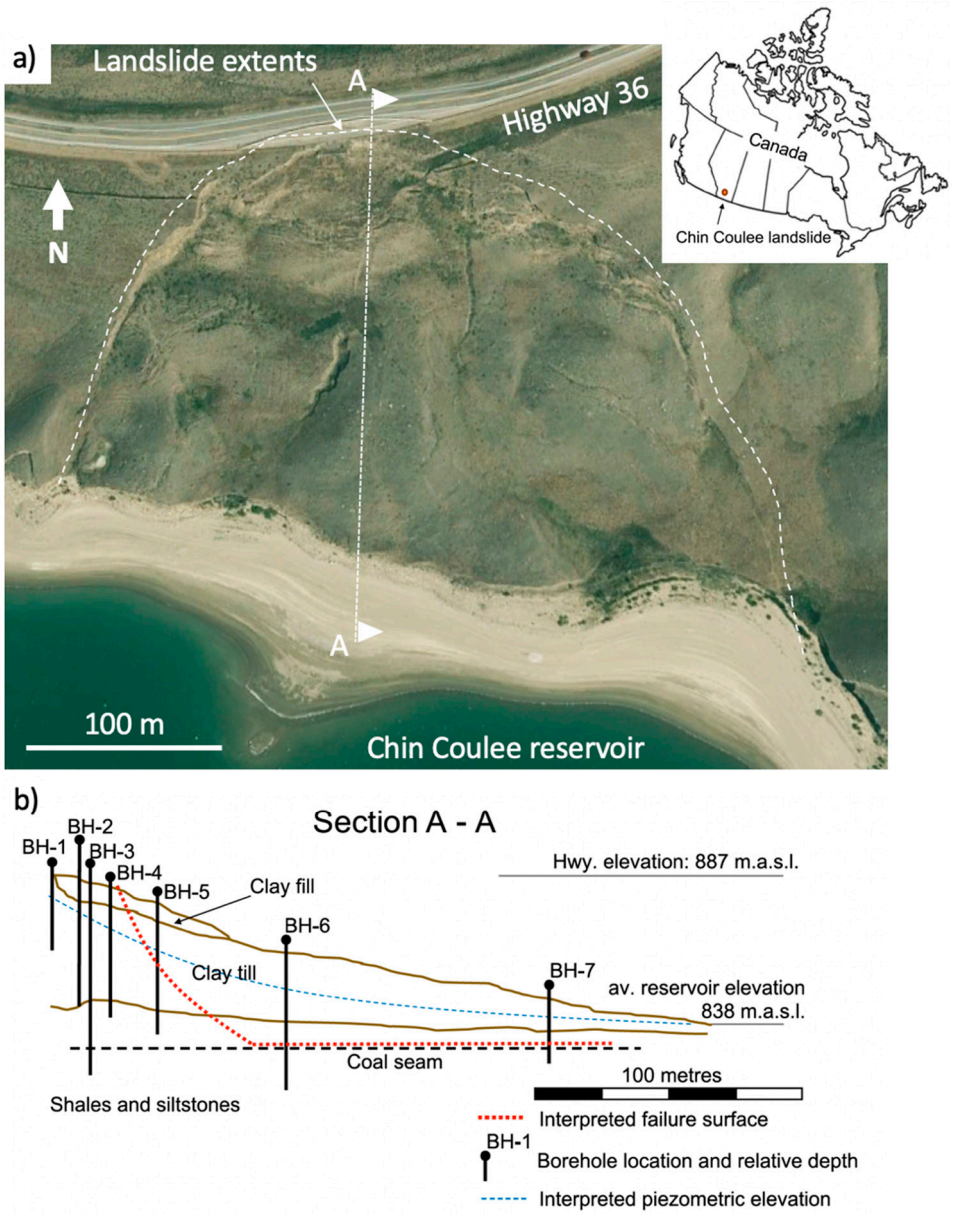

Figure 2. Location, aerial view (**a**) and typical geologic cross section (**b**) of the Chin Coulee landslide. Adapted from [30].

The local stratigraphy of the landslide is shown in Figure 2. Medium plasticity clay fill material from the initial highway construction and subsequent realignments and regrading is exposed at the head scarp of the landslide. A silty clay till with traces of fine gravel, mantles the valley slope. The till has low to medium plasticity and is very stiff to hard. The thickness of the till varies from approximately 20 m at the toe of the slope, to 35 m near the head scarp. Highly fractured shales and coal were encountered underneath the till [31]. The interpreted piezometric elevation is also shown in Figure 2. The landslide stratigraphy and piezometric elevation have been interpreted based on borehole logs (BH-1 to BH-7 in Figure 2), inclinometer readings (in BH-2, 3, 4 and 5), and piezometric readings (BH-1, 6 and 7) [30].

2.2. Landslide Extents and Deformation Patterns

The landslide extents were interpreted based on field and photographic mapping of the surface expression of the lateral failure surfaces and the head scarp. The landslide is approximately 350 m wide and up to 45 m deep. The length of the landslide is approximately

200 m long with the toe of landslide within the reservoir. The failure surface has been inferred based on the location of the head scarp, the shear zones identified in the slope inclinometers, and the location of a low-strength coal seam within the shales and siltstones (Figure 2). The total landslide volume is estimated at approximately 2 million cubic meters, based on measurement along the proposed failure plane and current landslide extents.

The Chin Coulee landslide has been interpreted as a translational retrogressive landslide seated within the highly fractured bedrock zone and sliding over the low-strength coal seam in Figure 2. Retrogression is inferred from surface tension cracks and concentrated deformations measured in the slope inclinometers near the head scarp. Displacement rates vary between 10 and 50 mm/year.

2.3. Instrumentation and Remote Sensing Techniques

Inclinometer readings are available for BH-2, 3, 4 and 5. Other instrumentation at the site includes a differential GPS system consisting of ten units (installed in July of 2018). This system is acquiring high frequency data, and details of its installation and interpretation can be found in [29]. Here, we will focus on the use of remote sensing techniques to obtain quantitative landslide information by leveraging historical aerial photography and state of practice remote sensing acquisition and processing.

Historic stereo pairs were available for 1945, 1960, 1970, 1982, 1993, 1999 and 2012. The stereopairs in 1982 had the more detailed scale (1:2500), with five photographs overlapping the scene of the landslide. These photographs were used to develop a surface model of the landslide using the software Pix4D (www.pix4d.com), and validated against the location of large boulders outside the landslide area that were assumed to be stable. The surface model was converted (sampled) to a point cloud with a minimum density of 500 points/m^2.

Laser scanning of the landslide was initiated in July of 2018 using a long-range scanner, ILRIS-LR, with a wavelength of 1064 nm, a pulse frequency of 10 kHz, and a beam divergence of 0.014324° [32]. Scanning was done from 3 locations across the reservoir from the landslide [29], with the average scan distance on Chin Coulee at 1000 m. The system has an accuracy of ±7 mm, which can be improved to ±4 mm through shot repetition and an averaging option. The scanner rendered over 8 million points, after removing tall vegetation and artificial structures and equipment. Point density ranged between 1000 and 2000 points/m2.

Quantitative information of the amount of slope deformation since the movement initiated was sought as a means to improve the understanding on the landslide kinematics for a better interpretation of the mechanisms behind the slope movement. Changes in the slope surface were calculated through comparing the point clouds from the 1982 aerial photographs and a laser scan from July 2019 (Change Detection). The software used for point cloud analysis and change detection was CloudCompare V2.10 (available through www.cloudcompare.org). The method used for change detection was M3C2 [33]. In the M3C2 method, change is quantified as the distance between point clouds measured parallel to the normal vector of the surface in the vicinity of each measurement point. The threshold for change detectability (limit of detection—LOD) was set at two standard deviations of measurements within areas considered stable (zero change). Changes calculated within ± two standard deviations were considered potential measurement randomness. The limit of detection between the 1982 photogrammetric model and the 2019 LiDAR model was 1 m, attributed to a lower accuracy of the 1982 model derived from historic photos and surficial changes between 1982 and 2019 due to erosional processes [30].

2.4. Results and Discussion

The results of the Change Detection between the 1982 photographs and the laser scanning in 2019 are shown in Figure 3 [30]. Negative values correspond to material loss and positive values correspond to movement towards the scanner (out of slope).

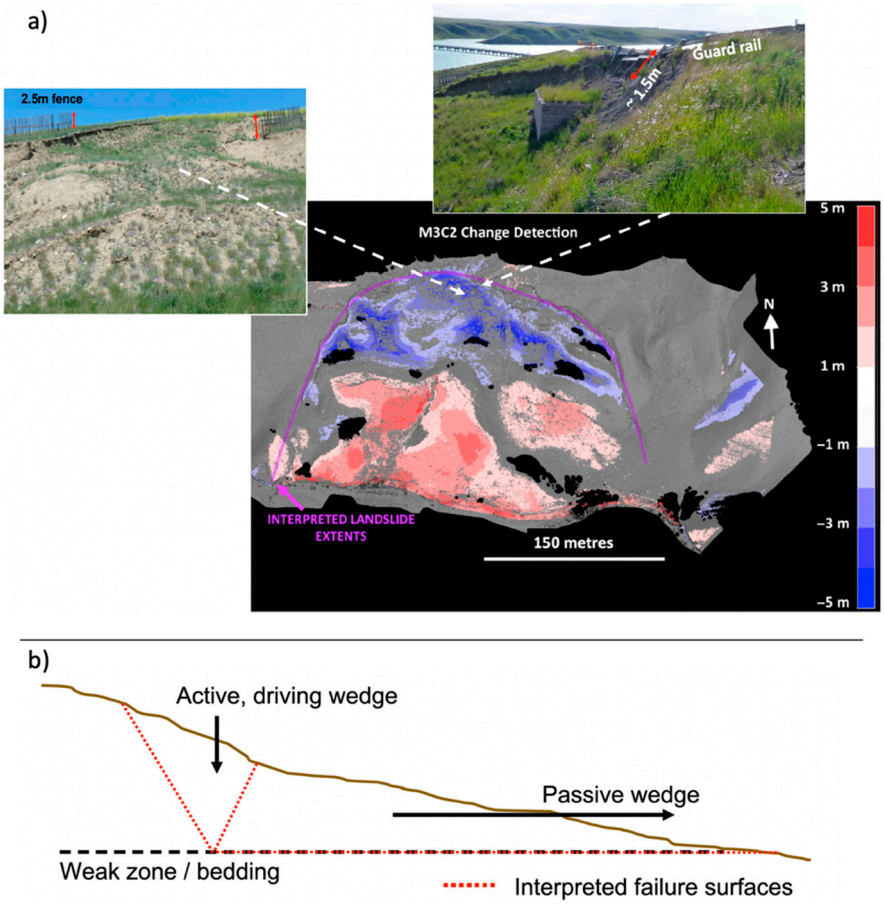

Figure 3. Change detection results at the Chin Coulee landslide (**a**) and interpreted landslide mechanism (**b**). Adapted from [30].

Loss of material in the upper half of the slope was measured at approximately 4 m between 1982 and 2019, which is validated by inspection of the landslide scarp when compared to a 2.5-m-high fence and a 1.5-m-long guardrail post (Figure 3a). Although there are differences in resolution and accuracy between the models, this comparison increased the confidence in the magnitudes of the calculated change for interpretation of the landslide kinematics. Changes in the lower half of the landslide suggest 2 to 3 m of outward movement at the toe of the slope (and up to 4 m in some areas). Unlike the gradational change in the direction of deformation expected from rotational landslides, the transition is sharp between the areas showing material loss (interpreted as downward movement of the landslide mass) and the outward displacement in the lower half of the landslide. This deformation trend is consistent with compound landslides mechanisms, where an active wedge moves downward (seen in the change as a loss of material) pushing a passive wedge outward on a sub-horizontal shear zone (seen in the calculated change as gain in material or movement towards the scanner). The sharp change to outward movement suggests the location of the contact between the driving and passive wedges (Figure 3) [30].

This enhanced knowledge regarding the mechanisms of the Chin Coulee Landslide allows improved determination of the slope stability as the reservoir fluctuates and evaluate the potential for sudden acceleration under reservoir increases and draw down conditions, supporting landslide risk evaluation under diverse scenarios.

3. Site C018

3.1. Location and Geology

Site C018 is a weathered rock slope adjacent to Highway 837 along the south bank of the Red Deer River, approximately 10 km northwest of the town of Drumheller, Alberta (Figure 4).

This slope is predominantly in a weak, poorly indurated sedimentary rock with layers of stronger sandstone, siltstone, and coal [34]. Bedrock is weak to extremely weak, with a UCS of less than 5 MPa and GSI of 20 to 25. The exposed bedding planes are visible in the valley slopes due to the variations of color and texture of the different materials. Bedding structures have an approximately sub-horizontal inclination of 10° [35].

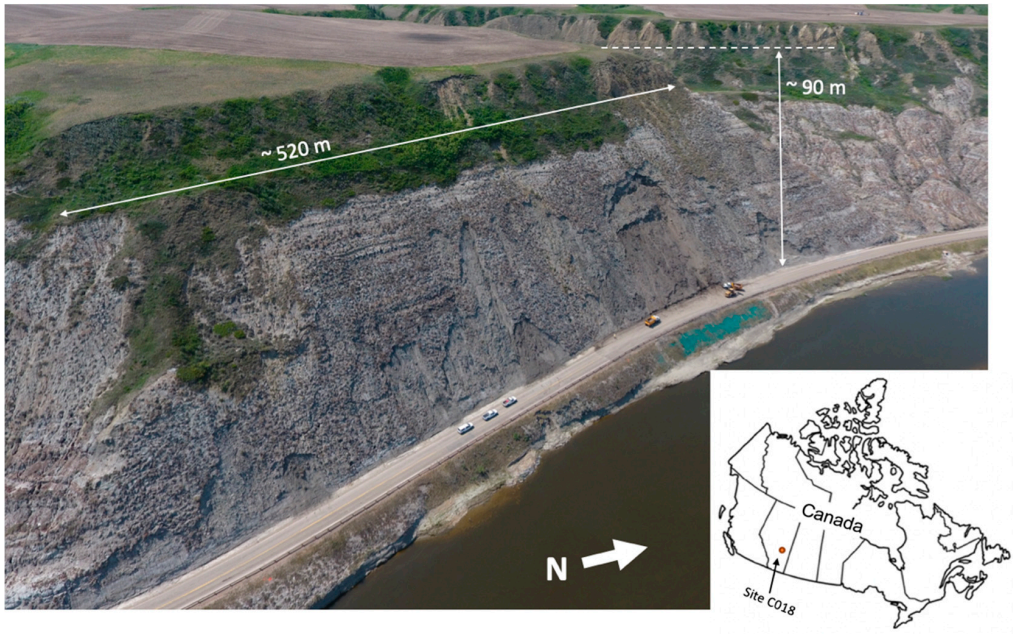

Figure 4. Location of the study site in Canada (lower right) and aerial view of Site C018.

The slope at site C018 shows extensive signs of weathering processes including deep gullies, sinkholes, weak runoff marks, and pipe erosion, where weathering processes are ubiquitous and result in a soft soil-like material at surface, with the bedrock structure almost eradicated. Discontinuous blocks of more indurated bedrock remain as less weathered rock blocks [34].

3.2. Landslide Extents and Deformation Patterns

Site C018 is a slope approximately 520 m long and 90 m high (Figure 4). This site has a long history of instabilities with fallen material reaching and blocking the highway. The slope displays three modes of failure, which largely depend on the moisture conditions of the materials forming the slope: (1) earthflows associated with heavy rainfall; (2) rock falls that result from differential weathering rates and undermining of various rock units; and (3) slides of frozen slabs of highly weathered rock [34].

3.3. Remote Sensing Technique and Analyses

Site C018 presents an example of the use of inexpensive unmanned aerial vehicle (UAV) photogrammetry as the basis for monitoring surface changes and for developing virtual surface models for geomorphic analysis (in this example, preferential drainage paths and rock fall trajectory models).

Three UAV photogrammetry surveys were conducted in December 2017, May 2018 and November 2018, respectively. The UAVs used in the surveys had a 12-MP (mega pixels) camera for the first and third flight and a 17-MP camera for the second flight. The 12-MP camera had a sensor 1/2.3″ CMOS (6.3 mm width and 4.7 mm height), a 94° field of view, a 20 mm focal length, and aperture f 1:2.8. The 17-MP camera had a sensor 1/2.3″ CMOS (6.3 mm width and 4.7 mm height), an 82° field of view, a 44 mm focal length, and aperture f 1:3.3. Minimum overlap between photographs was 60%, which required 655, 600 and 910 photographs for each of the three surveys in chronological order. Surface models

were developed using the software Pix4D and the surface model was converted (sampled) to a point cloud with a minimum density of 500 points/m^2 for Change Detection using the M3C2 method [35]. The surfaces were also used to develop a surface drainage network following the methods outlined in [36]; and for 2.5-dimensional rock fall trajectory simulations following the methods outlined in [37] and [38].

3.4. Results and Discussion

The results obtained by [35] are summarized in Figure 5. This figure shows the Change Detection between December 2017 and November 2018, the surface drainage model on the November 2018 surface model, and a plan view of rock fall trajectories on the November 2018 surface model.

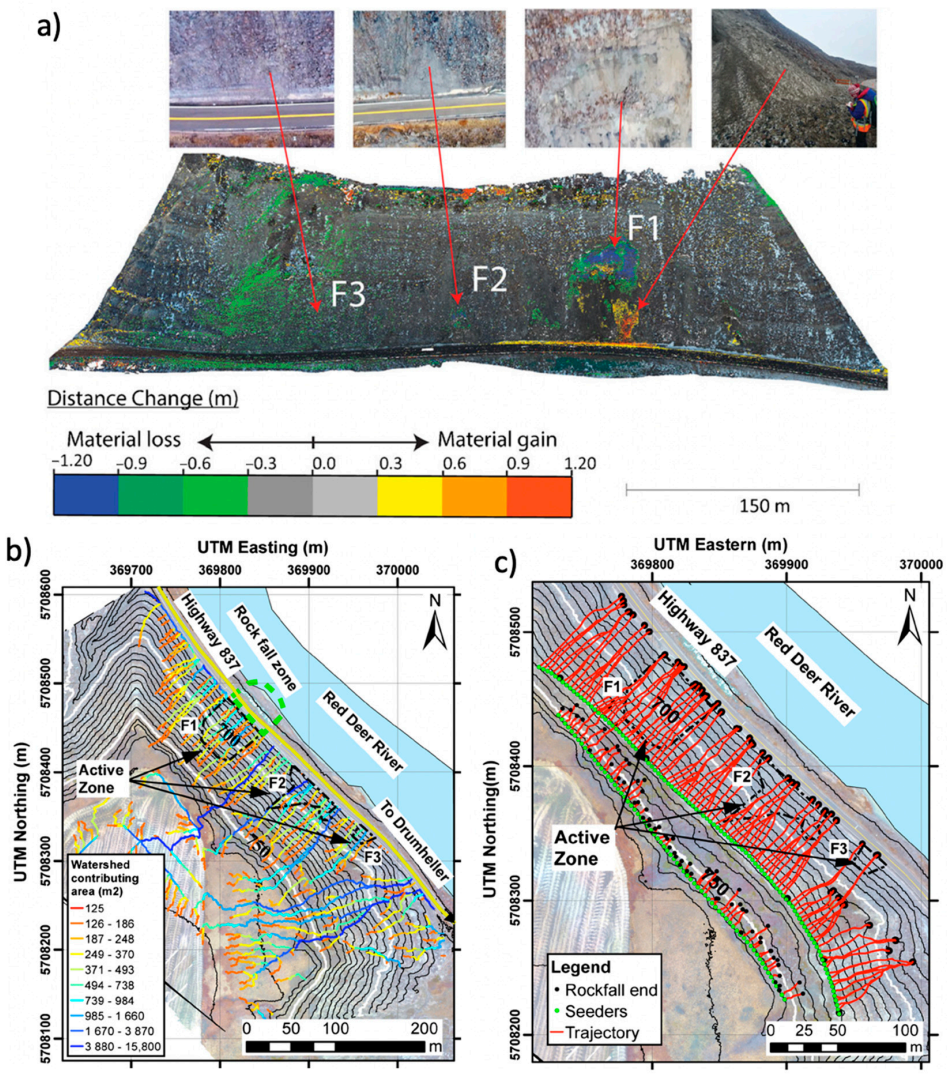

Figure 5. Change Detection between December 2017 and November 2018 (**a**), surface drainage model on the November 2018 surface model (**b**), and plan view of rock fall trajectories on November 2018 surface model (**c**). After [35].

The Change Detection results highlighted the state of activity of the areas of the slope that had recorded instabilities (Figure 5a–c). This analysis provided insight to prioritize area F1 for further hazard analysis, as some material was actively being eroded mid-slope and accumulating near the toe. This active erosion was more pronounced on weather-susceptible rock units, undermining stronger rock above, which could lead to rock fall events with the potential to reach the highway. This information, in combination with the

rock fall trajectory simulations in Figure 5c, allowed the development of hazard mitigation strategies at this site. The surface drainage models provided valuable information to evaluate the impact of surface runoff on the potential for earthflow occurrences. These results suggest surface water management strategies as one slope hazard and risk control option, diverting surface runoff away from the crest of the slope.

4. 10-Mile Slide

4.1. Location and Geology

The 10-Mile Slide is an active portion of a post-glacial earthflow, and is located in the Province of British Columbia, Canada, North of Vancouver [39] (Figure 6a). The landslide has been monitored for over 40 years, as its deformation has led to frequent maintenance of a highway and railway track that cross the continuously deforming mass.

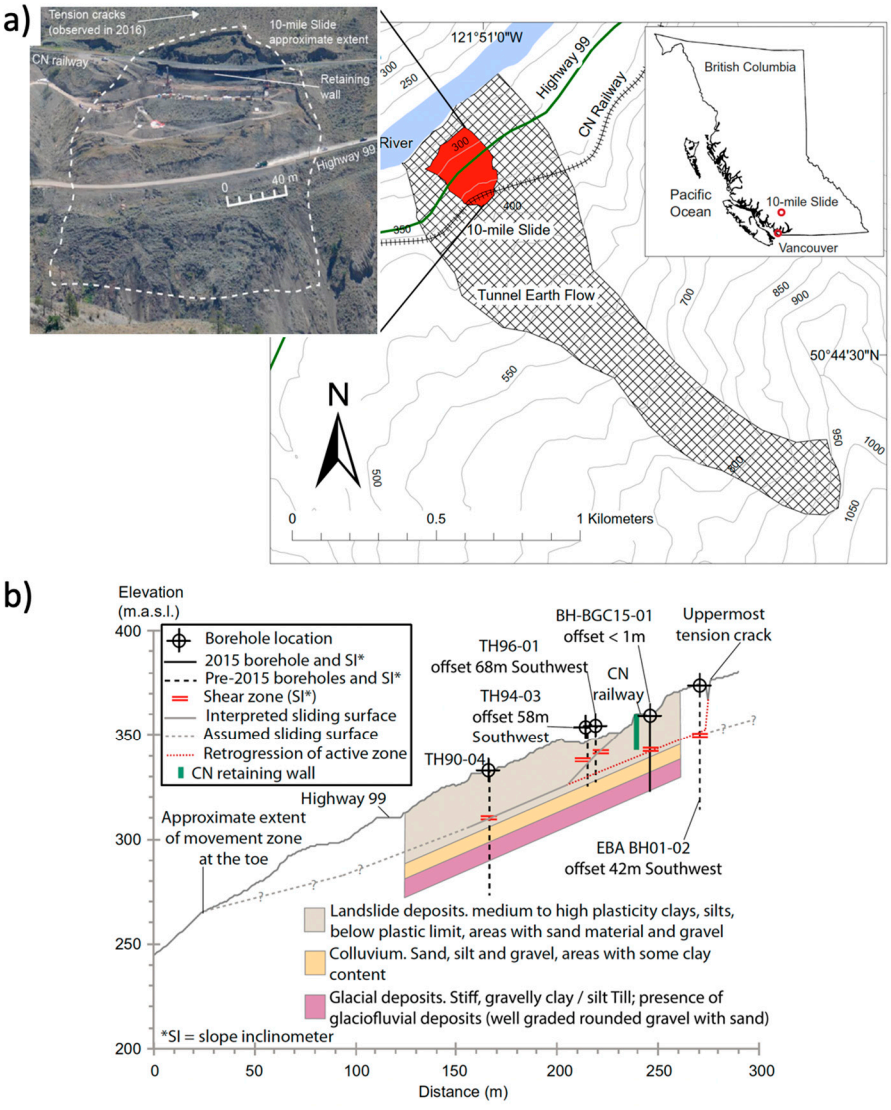

Figure 6. Location and front view of the 10-Mile Slide (**a**). Sketch of typical section and stratigraphy of the landslide (**b**) After [39].

The landslide is within the Fraser River valley, where glacial and post-glacial sediments are common along the valley slopes. The bedrock lithology in the area includes andesite to dacite volcanic rocks, sandstone, and shale. These rocks are overlain by quaternary deposits (including glacial drift blankets, colluvium, alluvium, and landslide deposits) [39,40]. This is reflected in the stratigraphy of the landslide, shown in Figure 6b,

which consists of a layer (up to 20 m thick) of mixed landslide deposits including medium to high plastic clays, silts, and the presence of zones of varying sand and gravel content. This layer overlies colluvium materials (sand, silt, and clay), which in turn overlie glacial deposits (stiff, gravelly clayey, and silty till with the presence of glaciofluvial well graded, rounded gravel, and sand deposits).

4.2. Landslide Extents and Deformation Patterns

The 10-Mile Slide is approximately 200 m wide and 140 m high, with an approximate volume of 750,000 m^3 [40]. Since the 1980s, displacement rates have varied spatially and temporally, with recorded rates up to 10 mm/day. The area of deformation was inferred from sharp scarps and tension cracks. The railway operator installed a 128-m-long retaining wall to control deformations, to an approximate depth of 16.5 m. and the highway operator has frequently realigned the highway as a response to the landslide movement.

The landslide is sliding on a continuous shear surface that extends upslope beyond the location of the railway tracks (Figure 6). This continuous shear surface appears to have a dip of approximately 22°, sub-parallel to the ground surface. Piezometers installed at different locations within the 10-Mile Slide have measured pore water pressure equal to or less than atmospheric pressure, suggesting that increases in pore pressures are not the driving mechanism for slope movements [39,40].

4.3. Instrumentation and Remote Sensing Techniques

Several slope inclinometers (SI) have been installed at the site. These were typically sheared within weeks of installation due to the fast deformation velocities [39]. Survey prisms (19 in total) were installed along the retaining wall and have been monitored since 2011. These were manually surveyed at different frequencies, with daily measurements in periods when the landslide showed the fastest deformation velocities. A differential GPS system consisting of 11 GPS units was installed in April of 2017 (same system to the one installed at the Chin Coulee Landslide). This system acquires high frequency data, and details of its installation and interpretation can be found in [41].

Ground-based (also terrestrial) laser scanning (TLS) was conducted in May and July of 2017 using a long-range scanner, ILRIS-LR, the same equipment used at Chin Coulee. Scanning was done from two locations across the river, with the average scan distance approximately 600m and a point density of approximately 1000 points/m^2 [41]. The point clouds from the TLS surveys were used for Change Detection with the software CloudCompare V2 and the M3C2 method (same procedures discussed before). The threshold for change detectability (limit of detection—LOD) was set at two standard deviations of measurements within areas considered stable; 5 cm in the case of the two scans.

4.4. Results and Discussion

The results of the Change Detection at the 10-Mile Slide between May and July of 2017 are shown in Figure 7. These results are shown together with the deformations measured by the GPS system between April and November of 2017. Figure 7a shows the location of the GPS units, together with the deformation vectors (to a scale of 1:500) and Figure 7b shows the cumulative deformations in selected units for the same period of time.

GPS monitoring showed that left and central areas of the landslide (North West side) have the highest displacement magnitudes (GPS units 46, 47 and 48). At the center of the landslide and near the highway cut, Unit 46 showed 400 mm displacement between April and November 2017. This is an order of magnitude larger than the units at the south-west end of the landslide. Similarly, Unit 43 showed displacement of approximately 30 mm during the same time frame.

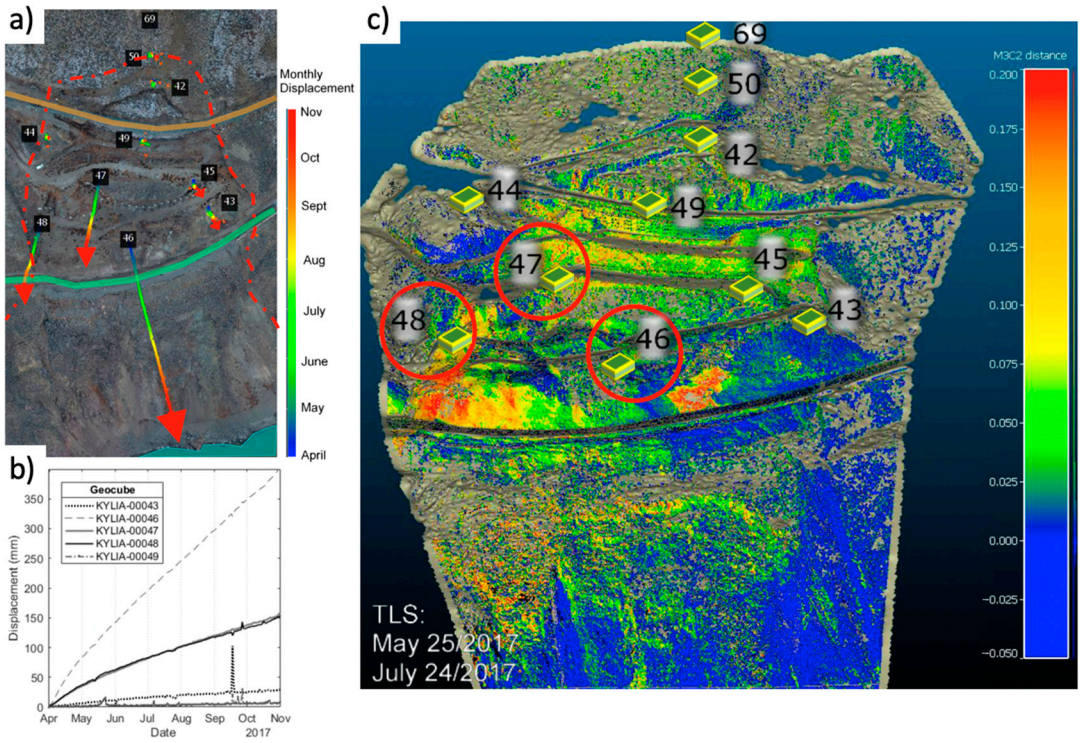

Figure 7. Location of GPS units and displacement vectors at a scale of 1:500 (**a**), cumulative displacements of selected units (**b**), and TLS Change Detection between May and July 2017 (**c**) After [41].

The results from Change Detection are compatible in magnitude with the GPS units (considering the two-month period between scans). At Unit 48, the cumulative displacement was 75 mm, with a range of 30 to 90 mm with Change Detection. At Unit 47, the displacement was 80 mm, with a range of 60 to 100 mm using Change Detection. At Unit 46, the cumulative displacement was 180 mm. However, Change Detection ranged between 50 and 125 mm. This difference near Unit 46 could be associated with the lower density of TLS points on this area due to the oblique angle of the LiDAR shot.

Importantly, the areas showing increased deformation within the landslide are consistent between both monitoring techniques. TLS Change Detection allows for better definition of the extent of the most active areas of the landslide, which allows for better interpretation of the landslide kinematics. It has been interpreted that an active block at the left side of the landslide toe is moving out of slope at a faster rate, leading to a decrease in the stability of the slope mass behind, which tends to follow the movements of the lower, left block. TLS Change Detection complemented with the detailed temporal resolution of the GPS Units allows for better interpretation of the landslide mechanisms, and therefore improved modeling of potential stabilization strategies. The setup also allows for the near real-time monitoring frequency required for landslide early warning systems.

5. Ashcroft Subdivision and the Ripley Landslide

5.1. Location and Geology

Fourteen landslides have been identified along a 10 km stretch of the Thomson River Valley, south of Ashcroft, British Columbia, Canada [42]. The location of this section of valley is shown in Figure 8.

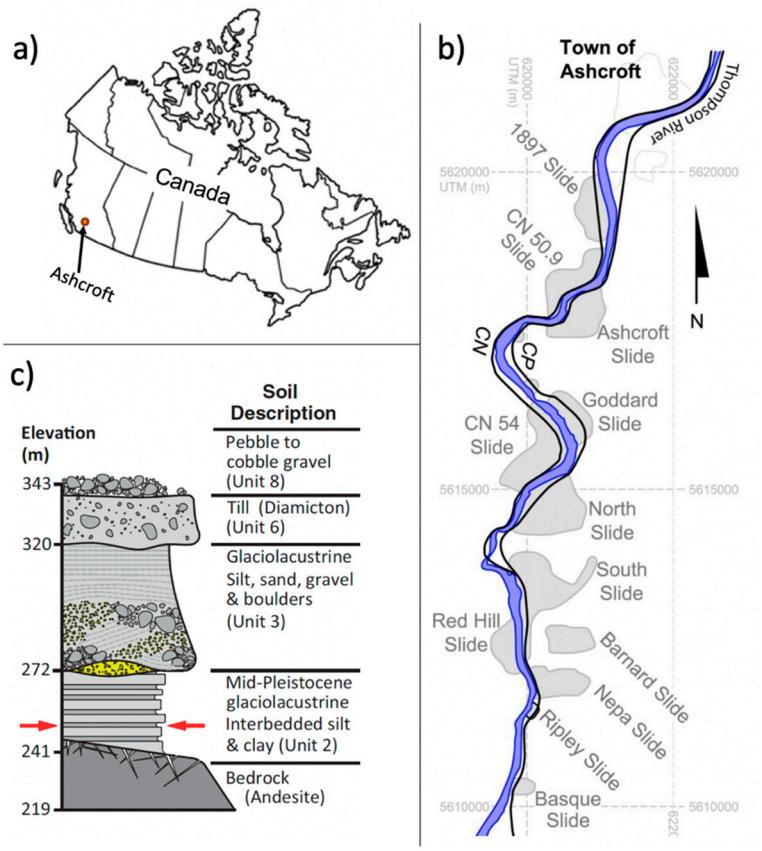

Figure 8. Location of landslides south of Ashcroft (**a**), detailed landslide layout (**b**), and stratigraphy in the area (**c**). Adapted from [42].

Eight soil units overlie andesitic bedrock in the study area [43]. These units were deposited by the advance and retreat of three glaciations (Figure 8). Unit 2 is comprised of highly plastic clay interbedded with glaciolacustrine silt (unit 2), heavily consolidated by glacial action. Unit 3 presents large quantities of silt, sand, gravel, and boulders near its base, also consolidated by glacial action. Unit 6 corresponds to glacial till (gravel size particles in a sandy, silty and clayey matrix). The stratigraphy of the valley is further complicated by an ancient Pleistocene river, which had cut down into unit 2, to the east of the current location of the Thompson River and deposits of boulders, gravels, and sands at depths below the interface of units 2 and 3 have been reported in borehole logs [42].

5.2. Landslide Extents and Deformation Patterns

The landslides in the 10 km section of the valley range in volume between 1 and 15 million m^3 and their velocities range from 4 to 30 mm/year to over 100 mm/year, although some have had faster displacement episodes of meters per day to meters per hour [42]. The areal extent of these landslides is shown in Figure 8b. These slides typically develop as compound slides, with an initial sliding mass that translates sub horizontally along the surfaces of rupture. The surfaces of rupture of the landslides through this section of the Thompson River Valley appear to occur along a common weak layer of clay located below the bottom of the river. After some movements, displaced masses become unstable and active wedges form at the main scarps. The weight of these wedges drives the mass towards the river [42].

One of these landslides, the Ripley Landslide, has been extensively investigated and shows an annual cycle of deformation accelerating in the Fall (September) and decelerating in the Spring (April), as a response to changes in river elevation. This landslide has shown annual deformations over 100 mm/year [42,44].

5.3. Instrumentation and Remote Sensing Techniques

Only a subset of these landslides have been instrumented, most with slope inclinometers that are manually read, annually. The Ripley landslide, however, has become a field laboratory for investigation and monitoring. Monitoring instrumentation at this landslide include grouted-in vibrating wire piezometers, inclinometer casings, Shape Accel Arrays (SAA), Differential GPS systems, and a wave-guide system that uses waves emitted as the landslide deforms and interprets them as relative displacement; among others. Site investigation techniques deployed at the site include borehole logging, geophysical investigations (seismic, electric resistivity), real time electric resistivity to calculate changes in unsaturated water contents, TLS and aerial laser scanning (ALS); among others [44–47]. Some of the in-place instrumentation at the Ripley Landslide are shown in Figure 9. These instruments have made it possible to arrive at the interpretation of the landslide kinematics as described above.

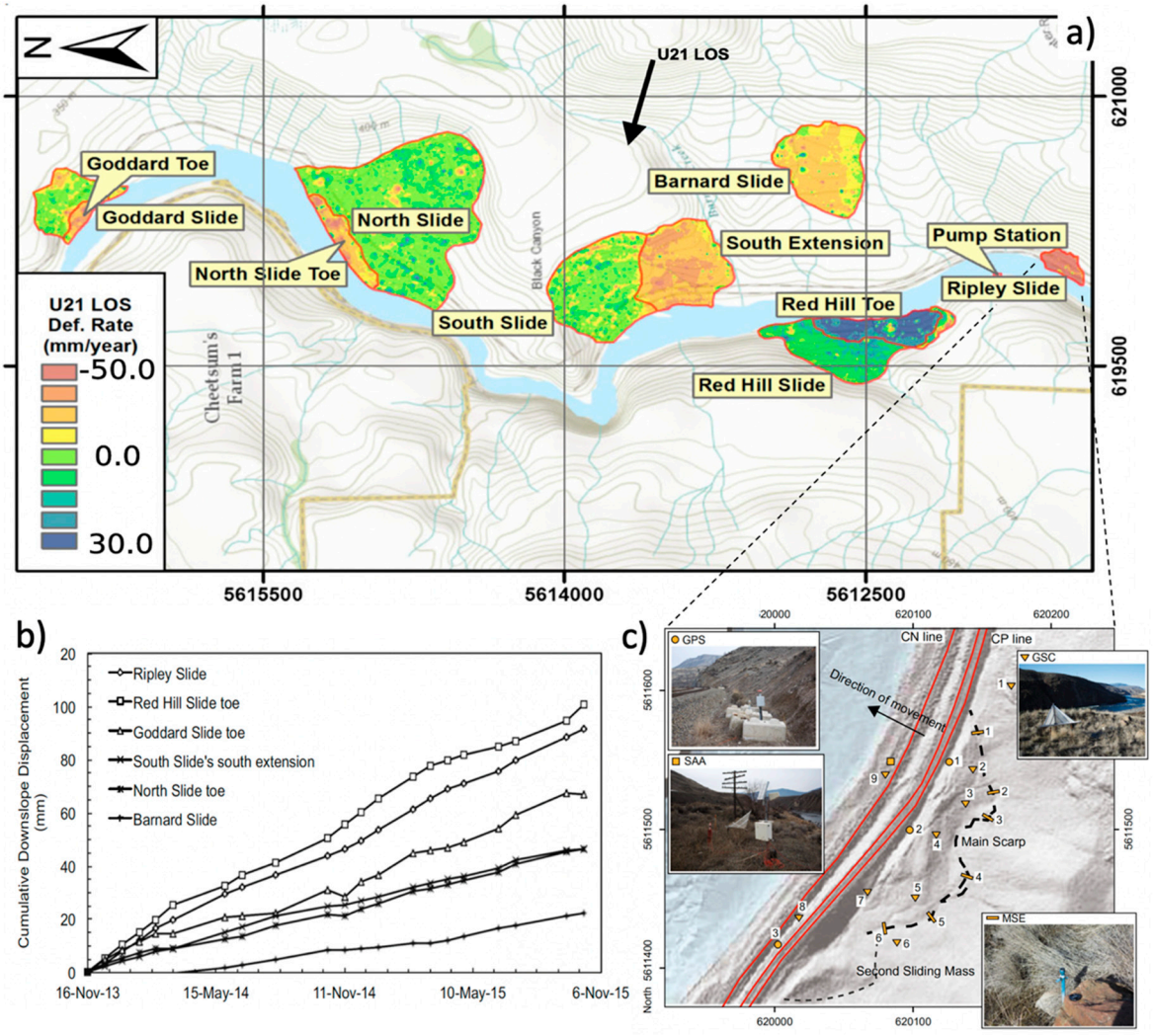

Figure 9. Line of Sight (LOS) displacement rates from Satellite InSAR at the active landslides (**a**,**b**). Location of some in-place instrumentation at the Ripley Landslide (GSE are corner reflectors, MSE are manual survey rods) (**c**). Adapted from [44,48].

Large-scale Satellite Interferometric Synthetic Aperture Radar (InSAR) was used in this section of the Thomson River Valley to understand the state of activity of slopes that are not being monitored at frequent as the Ripley Landslide, and potentially detect other active slopes not being monitored. The images used were captured by the Canadian satellite RADARSAT-2. East-facing images (group F4N) were collected between 2011 and

2015, and west-facing images (groups U5 and U21) were collected between 2013 and 2015. Images were acquired every 24 days, with some exceptions when longer gaps occurred. SAR images were processed using Persistent Scatterer Interferometry (PSI), and displacements measured are the average displacements for areas up to 15 m × 15 m [48].

5.4. Results and Discussion

The LOS displacement rate measured by the image group U21 at active landslides is shown in Figure 9 [48]. The average precision of measurements was 1 mm considering the Standard Deviation of measurements at stable areas.

The work in [48] used information about the LOS orientation of the satellite image groups and assumptions of the likely landslide displacement vectors based on the landslide kinematics prevalent in the area. Their analysis identified six areas of concentrated displacements within the study area, all within or adjacent to the footprints of identified landslides (Figure 9). Average LOS displacement rates ranged between 11 mm/year (Barnard) and 39 mm/year (Ripley Landslide). The maximum downslope displacement rate (Projection of the LOS to expected landslide displacement vector) was calculated at 120 mm/year (toe of the Goddard Slide). Maximum downslope displacements were between 73 and 89 mm/year for the other landslides, except for the Barnard Slide, with a maximum downslope displacement of 50 mm/year. Use of InSAR allowed the identification of landslides showing an Active state of activity, including the Ripley Landslide and the identification of an active mass adjacent to the South landslide (South Extension in Figure 9a), which had not been previously identified. It also allowed the identification of landslides potentially at a Reactivated state (Goddard Toe, Barnard, North Toe, and Red Hill landslides). These insights provide valuable information for an enhanced understanding of the corridor's risk level associated with potential landslide events and for improved landslide stability analyses for risk assessment purposes [49,50].

The InSAR analysis also identified that most of the Thompson River Valley landslides exhibit seasonal changes in the rate of displacement (median displacements particularly at the Ripley Landslide, Red Hill toe, Goddard toe, and South landslides). These typically show increased displacements during the late fall and winter months versus relative stability during the spring and summer. This suggests that factors that affect the stability of these landslides are common across the study area, and that these landslides are marginally stable [48].

6. Checkerboard Creek Rock Slope

6.1. Location and Geology

The Checkerboard Creek rock slope is located within the Revelstoke Reservoir, near the town of Revelstoke, British Columbia, Canada. Figure 10 shows the location of this landslide and a front view from across the reservoir.

The typical cross section in Figure 10 presents a sketch of the materials and structure forming the slope. Massive to weakly foliated granodiorite overlie gneiss and schist of a major regional fault system (Columbia River Fault), which has developed a broad, regional, brittle deformation zone of altered and mechanically deformed rock. Shears zones and joints in the slope are frequent, and dip steeply into and out of the slope at angles between 60° and 90° from horizontal. The rock mass quality ranges from very strong, fresh, undisturbed and blocky rock to highly weathered and altered, weak and disturbed. The lower quality rock masses contain frequent sheared and crushed zones and are typically found within 60 m of the slope surface [11,51].

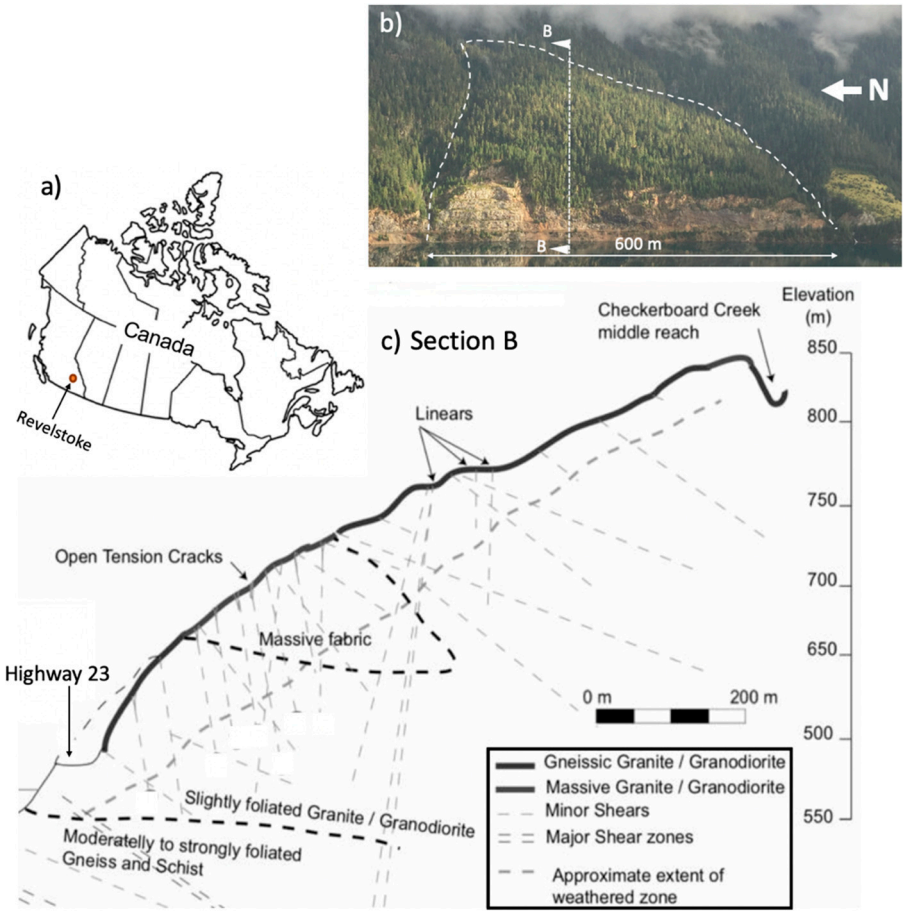

Figure 10. Location of the Checkerboard Creek rock slope (**a**) and front view (**b**). Typical cross section of the slope (**c**). Adapted from [11].

6.2. Landslide Extents and Deformation Patterns

The Checkerboard Creek rock slope is 260 m high, from Highway 23 to the middle reach of the Checkerboard Creek (Figure 10). The width of the slope is 600 m and the overall slope angle is 30°, steeper at the toe (45°) and flatter in the upper area (25°) [11]. The active zone of deformation has an average slope angle of 45°, and deformations have been detected down to 50 to 60 m deep. The volume of this active zone is estimated to be between 2 and 3 million m^3.

Slope deformations are concentrated at the central part of the slope, near the crest of the slope cut required to accommodate the highway. Displacements measured by instruments near the surface have revealed an annual cycle dominated by an active period from early October to April/May (early autumn throughout late winter), followed by a relatively quiet period between May and September (spring and summer). These cycles have been interpreted as temperature-dependent, where expansion and contraction of the rock blocks near the surface cause changes in the normal stresses at the contact of joint surfaces, and therefore changing the available shear strengths and deformation characteristics. Other instruments and measurements deeper into the active rock mass have shown steady rates of deformation [11,52,53]. The displacement rate is 0.5 mm/year at the boundaries of the actively deforming mass and up to 13 mm/year within the most active area. Deformation rates are greatest at the surface of the slope and decrease progressively, with depths to approximately 50 to 60 m below surface, where no deformations are detected. This depth coincides with the weathered and sheared volume of rock described above.

6.3. Instrumentation and Remote Sensing Techniques

The Checkerboard Creek rock slope has an extensive array of in-place instrumentation, mostly installed between 1984 and 2000. The instrumentation includes surface survey monuments (read annually), manual slope inclinometers (read annually) and in-place probes (read every 6 h), nested standpipe piezometers, multipoint borehole extensometers (read every 4 h), surface cable extensometers (read annually), strain meters, borehole and surface thermistors, and a weather station that records daily temperature and precipitation values [11,52]. A global navigation satellite system (GNSS) network has also been installed at the slope, which comprises of four sensors. Airborne laser scanning (ALS) was also carried out in September 2014 to acquire a high-resolution digital elevation model.

An IBIS-L GB-InSAR (ground-based, interferometric, synthetic aperture radar) manufactured by IDS Georadar was installed in October 2016 across the Revelstoke Reservoir from the Checkerboard Creek rock slope. The system has a radar head that acquires data as it travels on a 2-m-long rail to obtain a two-dimensional image from the area of interest (synthetic aperture). The system can target areas at distances of up to 4 km, covering a horizontal angle of up to 80°, and vertical angle of up to 40°. The resolution of the image therefore depends on the distance between the slope and the radar.

Challenges for system deployment include the inaccessibility to the electric power grid, which requires a self-sustained power supply. This is compounded with the climate of the site, which includes cold and dark winters, which decrease the solar power potential in the area and decreases the storage of the battery system. Given the very slow deformation rates of the Checkerboard Creek rock slope, and the challenges of power supply at the site, GB-InSAR monitoring was set at to D-InSAR mode (discontinuous, short duration monitoring campaigns), with monitoring campaigns of 1 to 2 weeks long [53]. Within each monitoring campaign, images were acquired at an average frequency of 6 images per hour. Due to the dense vegetation cover, GB-InSAR images were restricted to the exposed rock face adjacent to the highway.

6.4. Results and Discussion

The map of displacements in the LOS between the GB-InSAR and the Checkerboard Creek rock slope is shown in Figure 11. The extensive in-place instrumentation at the site allowed interpretation of temporal trends and insights into the spatial deformation patters; however, the GB-InSAR results allowed for an enhanced definition of the active portions of the exposed rock face. This active area detected by the GB-InSAR is bounded by the crest of the exposed rock face and the dark dashed line in Figure 11a. The average deformations in this area are consistent with those measured by in-place instruments. The threshold values used for identifying the most active area was 2 mm/year [52,53].

It was also identified that there is a transition between faster deformation rates near the crest of the expose rock face and its toe. This is consistent with the interpreted deformation kinematics in which the rock blocks within a heavily disaggregated rock mass are showing toppling like behavior and relative displacements between one another [53].

A critical insight from the GB-InSAR monitoring campaign was the identification of a potentially unstable block that appears to be sliding on a ledge defined by a persistent discontinuity that dips 15° to 20° out of slope (Figure 11). This newly identified potentially unstable block is within an area of the exposed rock face that was previously interpreted as less active. This block was most active between September 2016 and September 2017; however, it did not show increased activity when compared to the surrounding area after that period. This area of the exposed rock face was identified for continuous assessment as part of the slope's risk management system [53].

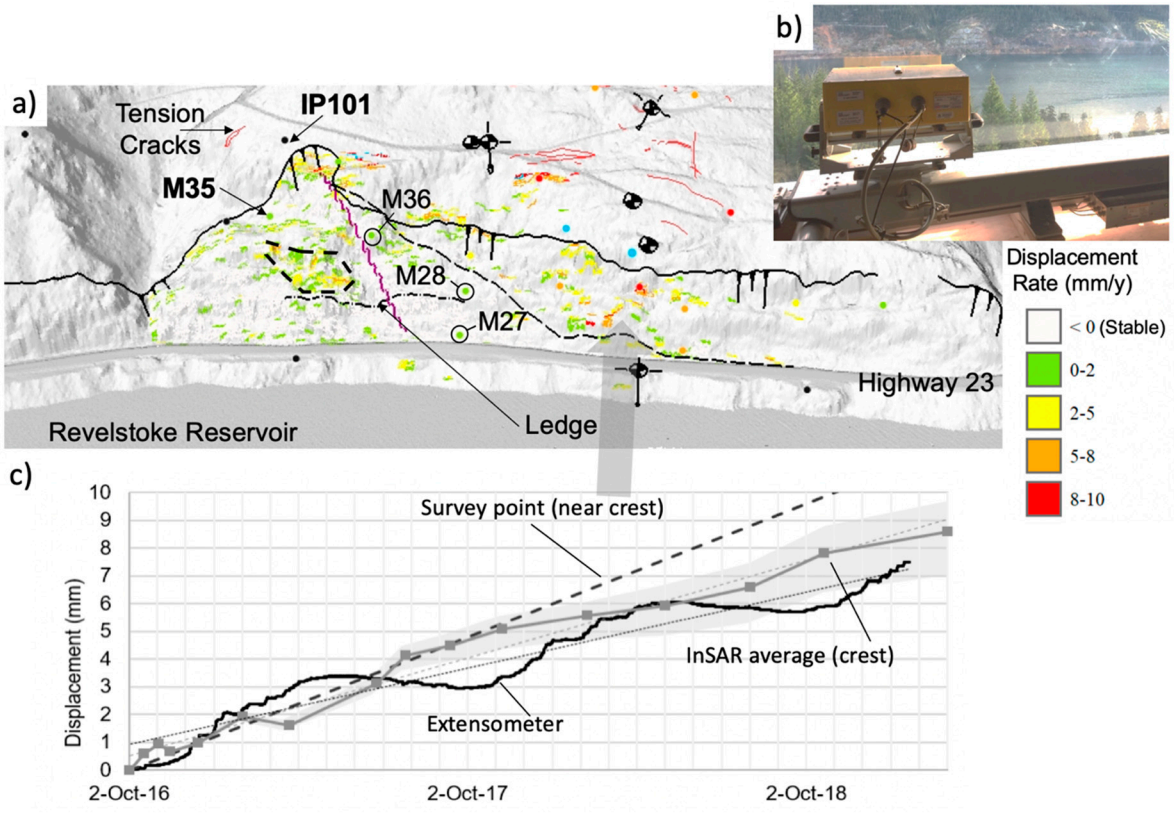

Figure 11. GB-InSAR displacement rate in the LOS at the Checkerboard Creek rock slope; crest of exposed rock face is shown with solid dark line, boundary of active deformation is shown in dark dashed line (**a**). View of the radar system looking towards the slope (**b**). D-InSAR average LOS displacement results for the active crest of the exposed rock face compared against a survey point and an extensometer located near the crest of the exposed rock face (**c**). Adapted from [53].

7. Tornado Mountain and S042 Site

7.1. Location and Geology

Tornado Mountain is north of the town of Sparwood, at the boundary between the provinces of British Columbia and Alberta, Canada. The study site corresponds to a steep rock outcrop on the British Columbia side, which in reality is part of Mount Lyne, adjacent to Tornado Mountain (Figure 12). The outcrop is 50 m high and near vertical, in strong, blocky limestone above a steep (approximately 45°) talus slope. The slope of the mountain side becomes gradually softer to an average of 22° as it approaches a railway alignment. This lower section of the slope is covered by rock fragments, soil, and is sparsely vegetated. This site has witnessed large blocks (up to 1.5 m in equivalent diameter) rolling downslope to the vicinity of the railway tracks [54].

The S042 Site is located adjacent to Highway 742, approximately 5 km southwest of Canmore, Alberta, Canada (Figure 12). This site consists of a near-vertical, 80-m-high rock slope on limestones, dolomitic limestones, dolostones and shale. Rock falls and erosional processes have created a talus slope of 40° between the slope and the highway. Rock falls mostly are captured on the talus slope; however; blocks of less than 0.3 m in equivalent diameter are commonly found on the road [55].

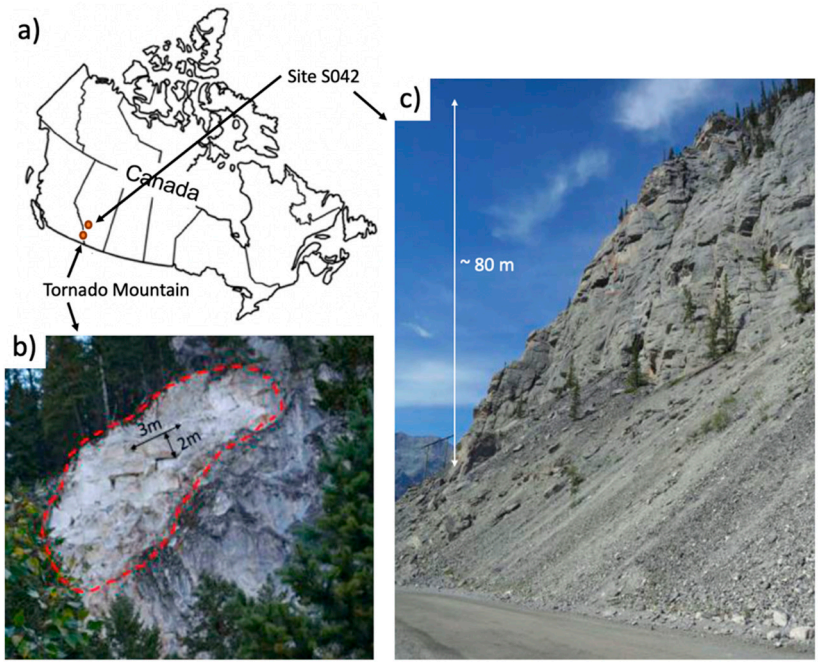

Figure 12. Location of the Tornado Mountain study site and S042 site (**a**). View of rock fall source at the Tornado Mountain site (**b**). View of the rock slope at S042 Site (**c**). Adapted from [55,56].

Both sites have been the matter of rock fall hazard investigations as part of assessments into the requirements and dimensioning of rock fall protection structures, for the railway tracks and highway 742 at the Tornado Mountain and Site S042, respectively. As part of these investigations, fragmented rock fall volume-frequency relationships were calculated on the basis of rock block surveys and photogrammetric techniques for virtual structural mapping (fragmented rock falls refer to fallen block volumes after detachment and disaggregation along their trajectory).

7.2. Photogrammetry and Structural Mapping

Ground-based photogrammetry at the study areas were performed with digital single-lens reflex (DSLR) cameras. The sensor size used was 35.9 mm by 24 mm, with 36.3 million pixels. The lens used at the Tornado Mountain site had a 200 mm fixed focal length and the lens used for Site S042 had a 150 mm fixed focal length. The distance between the camera and the slope were between 500 m and 600 m at the Tornado Mountain site, and between 200 m and 600 m at Site S042. The setup described rendered ground pixel sizes between 0.7 cm and 2 cm [56].

The photographs at both sites were processed in ADAM Technology's photogrammetry software suite (https://www.adamtech.com.au), which builds a digital surface model using photogrammetric principles and allows automatic and manual detection and mapping of rock structures. Orientations were mapped manually within the software for both sites.

The dip, dip direction and spacing of the sets of discontinuities were fitted to probability distributions and used to develop multiple iterations of discrete fracture networks (DFN) of persistent discontinuities for both sites using Wolfram's Mathematica software package (https://www.wolfram.com). These DFNs were used to calculate the fragmented rock fall volume-frequency distributions through numerical integration [56].

7.3. Results and Discussion

Ground-based, aerial and UAV photogrammetry have become standard practice for developing high-resolution surface models of rock slopes for structural mapping, both in civil and mining projects. This information is then used as input to estimate rock mass

characteristics (e.g., expected behavior and strength) and to develop geotechnical stability and hydrogeologic slope models. The analyses at Tornado Mountain and S042 Site are an example of how this information can also be used to calculate rock fall hazards in terms of volume-frequency curves. The method and results at Tornado Mountain and the S042 Site are detailed in [54,56]. A similar approach is described in [57] and tested for a rock fall site in Italy.

The results of the analyses at Tornado Mountain are shown in Figure 13. This figure shows the results of some steps of the analysis, including virtual mapping of discontinuities on the photogrammetric model (Figure 13a,b), as well as one iteration of the DFN developed based on the virtual mapping (Figure 13c) and the resulting fragmented rock fall volume-frequency curve (Figure 13d). Similar results were obtained for the S042 site (Figure 14). This figure shows the resulting discontinuity sets from virtual mapping in the photogrammetric model (Figure 14a), one iteration of the DFN developed based on the virtual mapping (Figure 14b), and the resulting fragmented rock fall volume-frequency curve (Figure 14c). Unfortunately, a view of the structures being mapped during the virtual mapping process was not available.

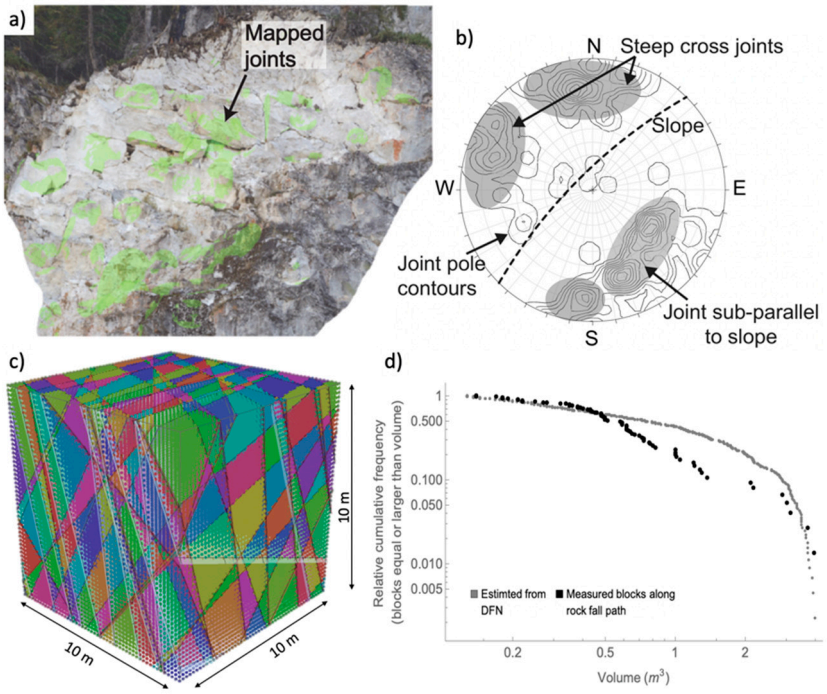

Figure 13. Virtual structural mapping (**a**) and resulting discontinuity sets (**b**) for the Tornado Mountain study site. One iteration of the DFN for the Tornado Mountain site (**c**). fragmented rock fall volume cumulative distribution based on the DFN realizations compared to block volumes surveyed along the rock fall trajectories, DFN volumes are truncated to the minimum range of surveyed block volumes for accurate comparison (lack of survey of small fraction of blocks) (**d**). Adapted from [55,56].

For the two cases analyzed, the rock fall volume-frequency relationships obtained with the DFN's were consistent with those from surveyed blocks. These results show that the approach could be used to estimate the fragmented rock fall volume–frequency relationships in the absence of rock fall records or block surveys along rock fall trajectories, as part of rock fall hazard and risk analyses. The approach presented in [54,56] was based on the hypothesis that fragmentation in strong rocks (particularly limestones characterized by Unconfined Compressive Strengths over 50 MPa) will tend to occur through weak planes and by extension of non-persistent discontinuities as the in situ blocks detach, fall,

bounce, and roll. In this regard the method should not be applied to other, weaker rocks, without validation.

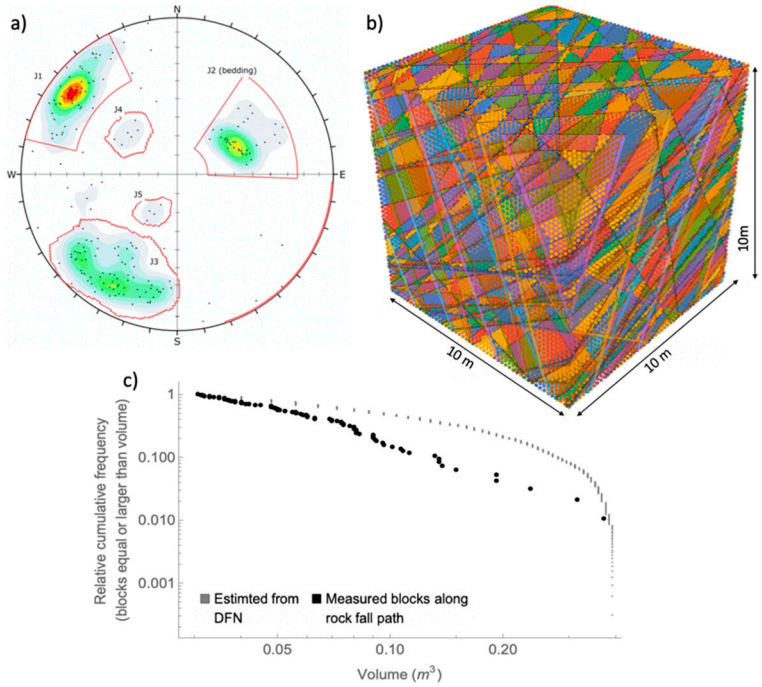

Figure 14. Discontinuity sets as a result of the virtual structural mapping (**a**) for the S042 Site. One iteration of the DFN for the S042 Site (**b**). Fragmented rock fall volume cumulative distribution based on the DFN realizations compared to block volumes surveyed at the toe of the talus slope, DFN volumes are truncated to the minimum range of surveyed block volumes for accurate comparison (lack of survey of small fraction of blocks) (**c**). Adapted from [56].

8. General Discussion and Conclusions

Monitoring plays a fundamental role in landslide risk management. Not only is robust monitoring the cornerstone of effective early warning, but also fundamental for increased understanding of the landslide mechanisms, kinematics and triggers. There is extensive experience in landslide site characterization and monitoring with the use of in situ testing, instrumentation, and remote sensing techniques; and technology keeps evolving such that instruments become more accurate and reliable. In this regard, remote sensing technologies have continued to develop to the point where they are becoming routine practice as part of landslide hazard and risk assessments and management. These include ground-based and airborne (from manned and unmanned aircrafts) photogrammetry, laser scanning, and satellite and ground-based radar interferometry [21–28]. This manuscript takes advantage of case studies from the authors' experience to illustrate the role of remote sensing approaches for implementing the systematic landslide risk management framework that has been widely adopted by industry [8–10,58].

Transportation corridors in Western Canada have to traverse the Canadian Cordillera and river valleys in the prairies, in which landslide hazards are common. The importance of these transportation corridors for the Canadian economy, and their vast extent, require cost effective techniques for landslide investigation and monitoring. Remote sensing techniques have been found to play a key role in achieving this. This paper synthesized six case studies in Western Canada from the authors' experience in which remote sensing was used in combination with other site investigation and monitoring technologies to gain understanding of the slope deformation mechanisms and develop early warning systems. These case studies cover different landslide types, including rock falls, compound soil and rock landslides, rock mass landslides, translational soil landslides and earth flows. Remote sensing techniques covered in these case studies include ground-based and satellite

InSAR, ground-based and UAV photogrammetry, as well as photogrammetry on historical photos, and ground-based laser scanning. This illustrates the versatility of remote sensing techniques for landslide investigation showing diverse kinematics and deformation mechanisms, as well as the diversity of available practical remote sensing techniques.

The case studies presented here demonstrate the deployment of remote sensing techniques for landslide investigation and monitoring, and how the most gain is obtained when complementing these techniques with information from other, more traditional in-place instrumentation (e.g., slope inclinometers, GPS units, survey prisms). The insights gained in these six case studies, including better definition of landslide deformation trends, both temporally and spatially, improvements in the understanding of landslide mechanisms, insights into rock fall volume-frequency distributions, and identification of the state of activity of large landside at a regional extent, among others. The insights illustrated in this manuscript are based on projects in civil engineering works; however, these are consistent with the reliance on remote sensing techniques by the mining industry to manage potential open pit slope failures. In this regard, remote sensing techniques have already been identified as essential for the successful implementation of open pit slope risk management framework [59]. It is the intent of the authors that these case studies will provide useful examples of the use of remote sensing techniques from a practical perspective and in a variety of contexts. It is noted that the work presented here reflects the methods that were considered most suited for the case studies discussed, which may vary in other contexts and for other jurisdictions. This work is not an exhaustive literature review of remote sensing techniques for landslide investigation; however, they present valuable examples for how the information captured from remote sensing techniques enhance the implementation of the landslide risk management framework.

Author Contributions: Both authors have contributed substantially to the manuscript and the work presented here. R.M. developed the conceptualization of the manuscript and selection of case studies. Both authors (R.M., M.T.H.) have provided the analysis presented in this paper, draft preparation, and visualization, as presented here. All authors have read and agreed to the published version of the manuscript.

Funding: The research work referenced in this review article was conducted through the (Canadian) Railway Ground Hazard Research Program, which is funded by the National Sciences and Engineering Research Council of Canada (NSERC ALLRP 549684-19), Canadian Pacific Railway, Canadian National Railway, and Transport Canada; and through a collaboration with Klohn Crippen Berger Ldt. and Alberta Transportation, funded by NSERC (Engage Gant # EGP 521877-17; KCB CRD # CRDPJ 543429-19) and KCB Engineering Inc.

Institutional Review Board Statement: Not applicable.

Informed Consent Statement: Not applicable.

Acknowledgments: The authors wish to acknowledge Canadian Pacific Railway, Canadian National Railway, Klohn Crippen Berger Ltd., Alberta Transportation and BC Hydro for their contributions to the work presented in this paper and for facilitating access to the sites, historic information and their invaluable experience. In particular, we thank the authors and co-authors of the references cited, which make the basis of the discussions and insights presented here.

Conflicts of Interest: The authors declare no conflict of interest.

References

1. Evans, S.G.; Hungr, O. The assessment of rock fall hazard at the base of talus slopes. *Can. Geotech. J.* **1993**, *30*, 620–636. [CrossRef]
2. Bunce, C.M.; Cruden, D.M.; Morgenstern, N.R. Assessment of the hazard from rock fall on a highway. *Can. Geotech. J.* **1997**, *34*, 344–356. [CrossRef]
3. Hungr, O.; Evans, S.G.; Hazzard, J. Magnitude and frequency of rock falls and rock slides along the main transportation corridors of southwestern British Columbia. *Can. Geotech. J.* **1999**, *36*, 224–238. [CrossRef]
4. Clague, J.J.; Evans, S.G. *Formation and Failure of Natural Dams in the Canadian Cordillera*; Geological Survey of Canada Bulletin: Ottawa, ON, Canada, 1994; Volume 464, 35 p.

5. Mansour, M.F.; Morgenstern, N.R.; Martin, C.D. Expected damage from displacement of slow-moving slides. *Landslides* **2011**, *8*, 117–131. [CrossRef]
6. Macciotta, R.; Cruden, D.; Martin, C.D.; Morgenstern, N.R.; Petrov, M. Spatial and temporal aspects of slope hazards along a railroad corridor in the Canadian Cordillera. In *Slope Stability 2013, Proceedings of the International Symposium on Slope Stability in Open Pit Mining and Civil Engineering, Brisbane, Australia, 25–27 September 2013*; Dight, P.M., Ed.; Australian Centre for Geomechanics: Perth, WA, Australia, 2013; pp. 1171–1186.
7. Fell, R.; Hartford, D. Landslide risk management. In *Landslide Risk Assessment, Proceedings of the International Workshop on Landslide Risk Assessment, Honolulu, Hawaii, 19–21 February 1997*; Cruden, D., Fell, R., Eds.; Balkema: Rotterdam, The Netherlands, 1997; pp. 51–108.
8. IUGS Working Group on Landslides; Committee on Risk Assessment. Quantitative risk assessment for slopes and landslides—The state of the art. In *Landslide Risk Assessment, Proceedings of the International Workshop on Landslide Risk Assessment, Honolulu, Hawaii, 19–21 February 1997*; Cruden, D., Fell, R., Eds.; Balkema: Rotterdam, The Netherlands, 1997; pp. 3–12.
9. Ho, K.K.S.; Leroi, E.; Roberds, W.J. Quantitative risk assessment application, myths and future direction. In *GeoEng2000, Proceedings of the International Conference on Geotechnical and Geological Engineering, Melbourne, Australia, 19–24 November 2000*; Technomic: Chicago, IL, USA, 2000; pp. 269–312.
10. Fell, R.; Ho, K.K.S.; Lacasse, S.; Leroi, E. A framework for landslide risk assessment and management. In *Landslide Risk Management, Proceedings of the International Conference on Landslide Risk Management, Vancouver, BC, Canada, 31 May–3 June 2005*; Hungr, O., Fell, R., Couture, R., Eberhardt, E., Eds.; CRC Press: Boca Raton, FL, USA, 2005; pp. 3–25.
11. Macciotta, R.; Martin, C.D.; Morgenstern, N.R.; Cruden, D.M. Development and application of a quantitative risk assessment to a very slow moving rock slope and potential sudden acceleration. *Landslides* **2016**, *13*, 765–785. [CrossRef]
12. Morgenstern, N.R. Toward landslide risk assessment in practice. In *Landslide Risk Assessment, Proceedings of the International Workshop on Landslide Risk Assessment, Honolulu, Hawaii, 19–21 February 1997*; Balkema: Rotterdam, The Netherlands, 1997; pp. 15–23.
13. Mostyn, G.; Sullivan, T. Quantitative risk assessment of the Thredbo landslide. *Aust. Geomech.* **2002**, *37*, 169–181.
14. Bonnard, C.; Forlati, F.; Scavia, C. (Eds.) *Identification and Mitigation of Large Landslide Risks in Europe—Advances in Risk Assessment*; Taylor and Francis Group: London, UK, 2004.
15. Lacasse, S.; Eidsvik, U.; Nadim, F.; Høeg, K.; Blikra, L.H. Event tree analysis of Aknes Rockslide hazard. In Proceedings of the 4th Canadian Conference on Geohazards: From Causes to Management, Canadian Geotechnical Society, Quebec City, QC, Canada, 20–24 May 2008; pp. 551–557.
16. Zhao, C.; Lu, Z. Remote sensing of landslides—A review. *Remote Sens.* **2018**, *10*, 279. [CrossRef]
17. Bianchini, S.; Herrera, G.; Mateos, R.M.; Notti, D.; Garcia, I.; Mora, O.; Moretti, S. Landslide activity maps generation by means of persistent scatterer interferometry. *Remote Sens.* **2013**, *5*, 6198–6222. [CrossRef]
18. Atzeni, C.; Barla, M.; Pieraccini, M.; Antolini, F. Early warning monitoring of natural and engineered slopes with ground-based synthetic-aperture radar. *Rock Mech. Rock Eng.* **2014**, *48*, 235–246. [CrossRef]
19. Tofani, V.; del Ventisette, C.; Moretti, S.; Casagli, N. Integration of remote sensing techniques for intensity zonation within a landslide area: A case study in the Northern Apennines, Italy. *Remote Sens.* **2014**, *6*, 907–924. [CrossRef]
20. Zhang, Y.; Meng, X.; Chen, G.; Qiao, L.; Zeng, R.; Chang, J. Detection of geohazards in the Bailong River basin using synthetic aperture radar interferometry. *Landslides* **2016**, *13*, 1273–1284. [CrossRef]
21. Bardi, F.; Raspini, F.; Frodella, W.; Lombardi, L.; Nocentini, M.; Gigli, G.; Morelli, S.; Corsini, A.; Casagli, N. Monitoring the rapid-moving reactivation of earth flows by means of GB-InSAR: The April 2013 Capriglio landslide (Northern Apennines, Italy). *Remote Sens.* **2017**, *9*, 165. [CrossRef]
22. Kromer, R.; Lato, M.; Hutchinson, D.J.; Gauthier, D.; Edwards, T. Managing rockfall risk through baseline monitoring of precursors using a terrestrial laser scanner. *Can. Geotech. J.* **2017**, *54*, 953–967. [CrossRef]
23. Lombardi, L.; Nocentini, M.; Frodella, W.; Nolesini, T.; Bardi, F.; Intrieri, E.; Carlà, T.; Solari, L.; Dotta, G.; Ferrigno, F.; et al. The Calatabiano landslide (southern Italy): Preliminary GB-InSAR monitoring data and remote 3D mapping. *Landslides* **2017**, *14*, 1–12. [CrossRef]
24. Novellino, A.; Cigna, F.; Sowter, A.; Ramondini, M.; Calcaterra, D. Exploitation of the intermittent SBAS (ISBAS) algorithm with COSMO-SkyMed data for landslide inventory mapping in north-western Sicily, Italy. *Geomorphology* **2017**, *280*, 153–166. [CrossRef]
25. Riquelme, A.; Cano, M.; Tomás, R.; Abellán, A. Identification of rock slope discontinuity sets from laser scanner and photogrammetric point clouds: A comparative analysis. *Procedia Eng.* **2017**, *19*, 838–845. [CrossRef]
26. Cucchiaro, S.; Cavalli, M.; Vericat, D.; Crema, S.; Llena, M.; Beinat, A.; Marchi, L.; Cazorzi, F. Monitoring topographic changes through 4D-structure-from-motion photogrammetry: Application to a debris-flow channel. *Environ. Earth Sci.* **2018**, *77*, 1–21. [CrossRef]
27. Gomez, F.; Rosenblad, B.; Loehr, E.; Smoot, J.; Lowry, B. Long-term monitoring of a slow moving landslide before and after remediation using ground-based radar interferometry. In Proceedings of the 2019 ASCE Geo-Congress GSP 311, Philadelphia, PA, USA, 24–27 March 2019.

28. Farina, P.; Catani, F.; Rosi, A.; Setiawan, I.; Junaidi, A.; Afrizal, K.; Wijayanto, A. Development of an early warning system for shallow landslide hazard in the Grasberg area, Indonesia. In Proceedings of the 2020 International Symposium on Slope Stability in Open Pit Mining and Civil Engineering, Perth, WA, Australia, 12–14 May 2020; Dight, P.M., Ed.; Australian Centre for Geomechanics: Perth, WA, Australia, 2020; pp. 1425–1438.
29. Deane, E.; Macciotta, R.; Hendry, M.; Gräpel, C.; Skirrow, R. The use and limitations of modern technologies for slow vegetated landslide monitoring—Chin Coulee landslide. In Proceedings of the 72nd Canadian Geotechnical Conference, Geo St. John's 2019, St. John's, NL, Canada, 29 September–2 October 2019.
30. Deane, E.; Macciotta, R.; Hendry, M.; Gräpel, C.; Skirrow, R. Leveraging historical aerial photographs and digital photogrammetry techniques for landslide investigation—A practical perspective. *Landslides* **2020**, *17*, 1989–1996. [CrossRef]
31. Deane, E.; Macciotta, R.; Hendry, M.; Gräpel, C.; Skirrow, R. Historical aerial photographs and digital photogrammetry techniques to investigate the development and evolution of the Chin Coulee landslide in Alberta. In *GeoVirtual 2020, Proceedings of the Canadian Geotechnical Conference, Calgary, AB, Canada, 14–16 September 2020*; Klohn Crippen Berger: Calgary, AB, Canada, 2020.
32. Teledyne Optech. ILRIS-LR Specifications Sheet. Available online: http://www.ticgroup.com.tw/menu/products/sur/products/3D_Laser/ILRIS%20LR.pdf (accessed on 7 December 2020).
33. Lague, D.; Nicolas, B.; Jérôme, L. Accurate 3D comparison of complex topography with terrestrial laser scanner: Application to the Rangitikei Canyon (N-Z). *ISPRS J. Photogramm. Remote Sens.* **2013**, *82*, 10–26. [CrossRef]
34. Roustaei, M.; Macciotta, R.; Hendry, M.T.; Rodriguez, J.; Gräpel, C.; Skirrow, R. Characterization of a rock slope showing three weather-dominated failure modes. In *Slope Stability 2020, Proceedings of the International Symposium on Slope Stability in Open Pit Mining and Civil Engineering, Perth, WA, Australia, 12–14 May 2020*; Dight, P.M., Ed.; Australian Centre for Geomechanics: Perth, WA, Australia, 2020; pp. 427–438.
35. Rodriguez, J.; Macciotta, R.; Hendry, M.T.; Roustaei, M.; Gräpel, C.; Skirrow, R. UAVs for monitoring, investigation, and mitigation design of a rock slope with multiple failure mechanisms—A case study. *Landslides* **2020**, *17*, 2027–2040. [CrossRef]
36. Jenson, S.K.; Domingue, J.O. Extracting topographic structure from digital elevation data for geographic information system analysis. *Photogramm. Eng. Remote Sens.* **1988**, *54*, 1593–1600.
37. Macciotta, R.; Martin, C.D.; Cruden, D.M. Probabilistic estimation of rockfall height and kinetic energy based on a three-dimensional trajectory model and Monte Carlo simulation. *Landslides* **2015**, *12*, 757–772. [CrossRef]
38. Macciotta, R.; Martin, C.D. Preliminary approach for prioritizing resource allocation for rock fall hazard investigations based on susceptibility mapping and efficient three-dimensional trajectory modelling. *Bull. Eng. Geol. Environ.* **2019**, *78*, 2803–2815. [CrossRef]
39. Carlà, T.; Macciotta, R.; Hendry, M.; Martin, C.D.; Edwards, T.; Evans, T.; Farina, P.; Intrieri, E.; Casagli, N. Displacement of a landslide retaining wall and application of an enhanced failure forecasting approach. *Landslides* **2018**, *15*, 489–505. [CrossRef] [PubMed]
40. Macciotta, R.; Rodriguez, J.; Hendry, M.T.; Martin, C.D.; Edwards, T.; Evans, T. The 10-mile slide North of Lillooet, British Columbia—History, characteristics and monitoring. In *Proceedings of the 3rd North American Symposium on Landslides, Roanoke, VA, USA, 4–8 June 2017*; Association of Environmental & Engineering Geologists (AEG): Brunswick, OH, USA, 2017; pp. 937–948.
41. Rodriguez, J.; Hendry, M.T.; Macciotta, R.; Evans, T. Cost-effective landslide monitoring GPS system: Characteristics, implementation and results. In Geohazards 7, Proceedings of the 7th Canadian Geohazards Conference, Canmore, AB, Canada, 3–6 June 2018. Available online: https://geohazardassociation.org/event/geohazards-7/ (accessed on 7 December 2020).
42. Hendry, M.T.; Macciotta, R.; Martin, C.D.; Reich, B. Effect of Thompson River elevation on velocity and instability of Ripley Slide. *Can. Geotech. J.* **2015**, *52*, 257–267. [CrossRef]
43. Clague, J.J.; Evans, S.G. Geologic framework of large historic landslides in Thompson River Valley, British Columbia. *J. Environ. Eng. Geosci.* **2003**, *9*, 201–212. [CrossRef]
44. Macciotta, R.; Hendry, M.; Martin, C.D. Developing and early warning system for a very slow landslide based on displacement monitoring. *Nat. Hazards* **2016**, *81*, 887–907. [CrossRef]
45. Macciotta, R.; Hendry, M.; Martin, C.D.; Elwood, D.; Lan, H.; Huntley, D.; Bobrowsky, P.; Sladen, W.; Bunce, C.; Choi, E.; et al. Monitoring of the Ripley landslide in the Thompson River Valley, B.C. In Proceedings of the 6th Canadian Geohazards Conference, Kingston, ON, Canada, 15–18 June 2014.
46. Huntley, D.; Bobrowsky, P.; Hendry, M.; Macciotta, R.; Best, M. Multi-technique geophysical investigation of a very slow-moving landslide near Ashcroft, British Columbia, Canada. *J. Environ. Eng. Geophys.* **2019**, *24*, 87–110. [CrossRef]
47. Huntley, D.; Bobrowsky, P.; Hendry, M.; Macciotta, R.; Elwood, D.; Sattler, K.; Best, M.; Chambers, J.; Meldrum, P. Application of multi-dimensional electrical resistivity tomography datasets to investigate a very slow-moving landslide near Ashcroft, British Columbia, Canada. *Landslides* **2019**, *16*, 1033–1042. [CrossRef]
48. Journault, J.; Macciotta, R.; Hendry, M.T.; Charbonneau, F.; Huntley, D.; Bobrowsky, P. Measuring displacements of the Thompson River valley landslides, south of Ashcroft, BC, Canada, using satellite InSAR. *Landslides* **2018**, *15*, 621–636. [CrossRef]
49. De Novellis, V.; Castaldo, R.; Lollino, P.; Manunta, M.; Tizzani, P. Advanced three-dimensional finite element modeling of a slow landslide through the exploitation of DInSAR measurements and in situ surveys. *Remote Sens.* **2016**, *8*, 670. [CrossRef]
50. Barra, A.; Solari, L.; Béjar-Pizarro, M.; Monserrat, O.; Bianchini, S.; Herrera, G.; Crosetto, M.; Sarro, R.; González-Alonso, E.; Mateos, R.M.; et al. A methodology to detect and update active deformation areas based on sentinel-1 SAR images. *Remote Sens.* **2017**, *9*, 1002. [CrossRef]

51. Stewart, T.W.G.; Moore, D.P. Displacement behaviour of the Checkerboard Creek rock slope. In *Terrain Stability in the Interior of British Columbia*; Technical Report 003; BC Ministry of Forests: Dawson Creek, BC, Canada, 2002.
52. Woods, A.; Hendry, M.T.; Macciotta, R.; Stewart, T.; Marsh, J. GB-InSAR monitoring of vegetated and snow-covered slopes in remote mountainous environments. *Landslides* **2020**, *17*, 1713–1726. [CrossRef]
53. Woods, A.; Hendry, M.T.; Macciotta, R.; Stewart, T.; Marsh, J. Updated understanding of the deformation characteristics of the Checkerboard Creek rock slope through GB-InSAR monitoring. *Eng. Geol.* **2021**, *281*, 105974. [CrossRef]
54. Macciotta, R.; Martin, C.D. Remote structural mapping and discrete fracture networks to calculate rock fall volumes at Tornado Mountain, British Columbia. In Proceedings of the 49th US Rock Mechanics/Geomechanics Symposium, San Francisco, CA, USA, 28 June–1 July 2015.
55. Macciotta, R.; Gräpel, C.; Keegan, T.; Duxbury, J.; Skirrow, R. Quantitative risk assessment of rock slope instabilities that threaten a highway near Canmore, Alberta, Canada: Managing risk calculation uncertainty in practice. *Can. Geotech. J.* **2020**, *57*, 337–353. [CrossRef]
56. Macciotta, R.; Gräpel, C.; Skirrow, R. Fragmented rockfall volume distribution from photogrammetry-based structural mapping and discrete fracture networks. *Appl. Sci.* **2020**, *10*, 6977. [CrossRef]
57. Francioni, M.; Antonaci, F.; Sciarra, N.; Robiati, C.; Coggan, J.; Stead, D.; Calamita, F. Application of unmanned aerial vehicle data and discrete fracture network models for improved rockfall simulations. *Remote Sens.* **2020**, *12*, 2053. [CrossRef]
58. Lacasse, S. Hazard, reliability and risk assessment—Research and practice for increased safety. In Proceedings of the 17th Nordic Geotechnical Meeting, Reykjavik, Iceland, 25–28 May 2016; pp. 17–42.
59. Sharon, R.; Eberhardt, E. *Guidelines for Slope Performance Monitoring*; CRC Press, Taylor & Francis Group: Leiden, The Netherlands, 2020.